Electron-scattering studies of carbonyl fluoride

Jaspreet Kaur,[1] Nigel Mason,[2] and Bobby Antony[1,*]

[1]*Atomic and Molecular Physics Laboratory, Department of Applied Physics, Indian School of Mines, Dhanbad 826004, Jharkhand, India*

[2]*Department of Physics & Astronomy, The Open University, Milton Keynes MK7 6AA, United Kingdom*

(Received 8 July 2015; revised manuscript received 2 October 2015; published 3 November 2015)

The present article reports calculations of total, momentum transfer, differential, excitation, and ionization cross sections for electron scattering from the carbonyl fluoride (F_2CO) molecule. Total cross sections (TCSs) are presented over an extensive energy range from 0.5 to 5000 eV. The *ab initio R*-matrix and spherical complex optical potential methods were used to perform low-energy computations and intermediate- to high-energy calculations, respectively. The TCSs computed through these two formalisms are in good agreement in the 24–26 eV energy range. The consistency of the data in this overlapping region has allowed us to predict total cross sections over an extensive energy range. Electronic excitation, momentum transfer, and differential cross sections were also calculated using the *R*-matrix method at low incident energies. In the present study, a low-energy resonance at 3.67 eV was detected with a $^2B_1$ symmetry, indicating the probability of anion formation by the dissociative electron attachment process and further decay to neutral and negative ion fragments. The total ionization cross section for F_2CO was also evaluated using the complex scattering potential–ionization contribution method and the binary encounter Bethe method up to 5 keV.

DOI: 10.1103/PhysRevA.92.052702 PACS number(s): 34.80.Bm, 34.80.Ht, 34.50.Gb

I. INTRODUCTION

Carbonyl fluoride (F_2CO) is of current interest in relation to the atmospheric degradation of hydrofluorocarbon (HFC) 134a (CF_3CH_2F), the replacement refrigerant for CFCs [1], and the thermal degradation of the multipurpose perfluoropolyethers. Recently, Mitsui *et al.* have suggested F_2CO as a more suitable chamber-cleaning agent than conventional perfluoroethane (Freon 116, C_2F_6), in plasma-enhanced chemical vapor deposition due to its reduced global warming potential (GWP) arising from its quick hydrolysis to form CO_2 and HF in the troposphere [2]. In solar cell manufacture carbonyl fluoride is used as a plasma feed gas, at atmospheric pressure or higher. F_2CO is also applied to selectively etch silicon oxide in silicon oxide–silicon composites [3]. Atmospheric concentrations of F_2CO may therefore increase in future years due to the adoption of F_2CO by industry and due to its creation by the reaction $CF_3O + NO \rightarrow F_2CO + FNO$, the only prominent product channel in terminating ozone-depleting catalytic channels of the CF_3O radical in the stratosphere where it is formed indirectly by emissions from HFCs [4]. Such industrial and environmental importance of F_2CO has therefore led to renewed interest in the physical and chemical properties of this molecule.

There have been numerous ultraviolet, photoelectron, and VUV photoabsorption studies on the F_2CO molecule. However most of these studies were performed four decades ago and are documented in Refs. [5–11] and references therein. In 1978, Vasudevan and Grein [12] investigated the vertical electronic spectrum of F_2CO in considerable detail and reported vertical excitation energies corresponding to different singlet and triplet excited states. Sherwood *et al.* [13] recorded the He I and II photoelectron (PE) spectra of the carbonyl dihalides to study the electronic structure of F_2CO. Meanwhile, Grein [14] performed an extensive theoretical analysis of the UV and photoelectronic spectra of F_2CO by employing the multireference configuration-interaction method. A few years later, Olalla *et al.* [15] computed the spectral intensities of ns ($n = 3$–12) Rydberg transitions in carbonyl compounds with the molecular adapted quantum defect orbital procedure. Choi and Baeck [16] performed calculations using the coupled-cluster and equation-of-motion coupled-cluster singles and doubles (CCSD and EOM-CCSD) methods to study the spectroscopic constants of the ground and low-lying excited states of X_2CY (X = F, Cl, Cl; Y = O, S).

Kato *et al.* [17] were the first to publish high-resolution data on electron-impact vibrational excitation for two of the six fundamental modes of F_2CO. In 2011, the first complete electron energy-loss spectra (EELS) of carbonyl fluoride was measured by Kato *et al.* [18] from 5.0 to 18.0 eV. They assigned the observed EELS of F_2CO to a combination of valence and Rydberg transitions on the basis of available comparisons of vertical excitation energies and oscillator strengths for this molecule. In the same year, Hoshino *et al.* [19] investigated the low-energy electron attachment to gas-phase carbonyl fluoride from 0 to 30 eV, by means of a tunable electron source assembled directly at the entrance of a quadrupole mass spectrometer. They performed quantum chemical calculations at the Becke-three parameter-Lee-Yang-Parr (B3LYP) augmented correlation-consistent polarized valence triple zeta (aug-cc-pVTZ) level of theory for the same to validate their results. The capture of low-energy electrons in the energy range 2.0–2.6 eV by F_2CO is assigned to the formation of different dissociative electron attachment (DEA) fragments obtained by Gaussian fitting profiles. Thus, it is quite evident that F_2CO has been the subject of theoretical and experimental studies for a long time; however, there are almost no data deriving the magnitude of electron-scattering cross sections from F_2CO. The present investigation on electron-scattering cross sections of F_2CO was therefore to establish a reference set of electron-scattering data from F_2CO in view of its importance in various applied and pure sciences and the lack of cross section data.

*bka.ism@gmail.com

The electron-impact cross section calculations were carried out using two distinct formalisms, since a single formalism which can be applied to a wide energy from 0.5 to 5 keV does not exist. The low-energy calculations up to 30 eV were performed using the *ab initio R*-matrix [20] method through the QUANTEMOL-N package [21], while at higher energies the spherical complex optical potential (SCOP) formalism [22–25] is used. Both formalisms are well established and are consistent over their respective energy ranges. Hence, the main aim of the present work is to predict target parameters, detect resonances, if any, at low energies, and to provide electron-impact scattering cross sections over an extensive range of impact energies.

Besides the *R* matrix, several other close-coupling formalisms are used for low-energy scattering calculations of molecules, such as the Schwinger multichannel method [26], the complex Kohn variational method [27], and the linear algebraic method [28]. All these methods are competent to describe the scattering phenomena at low energies and are well established. The *R*-matrix formalism gives accurate results at low energies and is used to calculate the differential, excitation, momentum transfer, and total cross sections up to 30 eV. The *R*-matrix method is also extremely useful in predicting target parameters and detecting resonances. A resonance may be associated with a temporary bound state of an electron with a molecule that is formed by an effective potential well. The temporary bound state is an excited state of a negative ion, i.e., the system of the neutral molecule plus the electron which may or may not be bound in the ground state. Thus the electron becomes temporarily trapped in the molecular orbital, which may lead to fragmentation of the molecule into neutral and negative ions by the dissociative electron attachment process. DEA depicts a comprehensive idea about the local chemistry occurring during an electron-molecule interaction. The intermediate- to high-energy total elastic and total inelastic cross section calculations are performed using the Spherical Complex Optical Potential (SCOP) formalism [22–25]. For the total ionization computations, a semiempirical method called the Complex Scattering Potential–ionization contribution (CSP-ic) [29–31] is employed.

The next section will present a detailed description of the theoretical methodology adopted in the present work.

II. THEORETICAL METHODOLOGY

The fixed-nuclei approximation is used to describe the electron-scattering calculations at the equilibrium geometry of the molecule. The accurate *ab initio R*-matrix code [20] is used for calculations from 0.5 to 30 eV using the QUANTEMOL-N package [21]. Conventionally, the *R*-matrix method is applied up to 15 eV. However, we have extended the calculations to 30 eV and the cross section shows two broad peaks at 17 and 24 eV. The SCOP and CSP-ic methodologies are primarily high-energy formalisms and are used for calculations above the ionization potential of the target. The SCOP method [22–25] is employed for calculation of total elastic and inelastic cross sections. The total ionization cross section is derived from the total inelastic cross section from a semiempirical CSP-ic method [29–31].

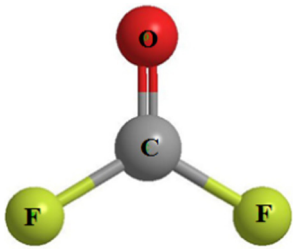

FIG. 1. (Color online) Structure of carbonyl fluoride.

Before proceeding to the details of the theoretical methods used, the target model is discussed here. The target model entails the discussion of target properties, symmetry, and the equilibrium configuration of the molecule. A more precise representation of the target's properties ensures a more accurate representation of the target and hence leads to a better evaluation of the final cross sections.

A. Target model

Figure 1 shows the equilibrium molecular structure of F_2CO. Carbonyl fluoride, like its analog phosgene, is planar with C_{2v} point group symmetry of the order 4 (Fig. 1). The calculations were performed using the cc-pVTZ basis set which gave the best target parameters, especially the dipole moment (0.89 D), which is reasonable considering the available data (Table I). This suggests that the cc-pVTZ basis set generates the best wave functions and hence it is used to calculate various cross sections. The target geometry is obtained from the Computational Chemistry Comparison and Benchmark Database (CCCBDB) [32].

The ground-state Hartree-Fock electronic configuration of F_2CO is $1b_2^2,1a_1^2,2a_1^2,3a_1^2,4a_1^2,2b_2^2,5a_1^2,6a_1^2,3b_2^2,1b_1^2,7a_1^2,1a_2^2,4b_2^2,8a_1^2,2b_1^2,5b_2^2$. For viable scattering calculations, an effort should be made to minimize the number of electrons in the active region without losing vital information. In view of this, eight electrons are kept in the active space and the remaining 24 electrons are frozen in the configuration space of the molecule. The orbitals corresponding to active space are comprised of $8a_1,9a_1,10a_1,2b_1,3b_1,4b_1,4b_2,5b_2,6b_2$, whereas the frozen orbitals are $1a_1,2a_1,3a_1,4a_1,5a_1,6a_1,7a_1,1b_1,1b_2,2b_2,3b_2,1a_2$. Eleven target states are employed in the

TABLE I. Target properties.

Property	Present result	Experiment	Theory
Ground-state energy (hartree)	−311.76		−311.74 [32]
First Excitation energy (eV)	7.82		7.35 [14] 7.20 [16] 7.47 [17]
Rotational constant (cm^{-1})	0.394	0.394 [8] 0394 [33]	0.394 [32]
Dipole moment (D)	0.89	0.91 [8] 0.95 [34]	1.03 [19] 0.95 [35]

close-coupling expansion and retained in the outer region. The present calculations include 71 scattering channels and 1386 configuration-state functions in the ground state. The computed target properties using the current model are in good accord with the available comparisons (Table I).

B. Low-energy formalism

Within the *R*-matrix method, there is a separation of space into two regions by considering the nature of the interactions between the scattering electron and the target system. This is achieved by enclosing the target inside an imaginary sphere, large enough to contain the entire *N*-electron target wave function. Outside this sphere, the electron and the target can be described by their long-range multipolar interactions. In the present calculations the radius of the inner region is taken as $13a_o$ and has been chosen such that it encloses the entire charge density of the molecule. The description of the $(N + 1)$ wave function of the electron and the target system within the sphere takes care of the exchange and correlation effects among all the $N + 1$ electrons. The description of short-range electron interactions in this region is sophisticated and the *R*-matrix method is realized numerically by the adaptation of quantum chemistry codes. The *R*-matrix method is advantageous as the inner-region Hamiltonian is independent of the scattering energy and is solved only once. In contrast, the outer region is energy dependent and computationally cheap. The radius of the outer region is kept fixed at $100.1a_o$. Here, a single-center close-coupling approximation is employed for the long-range multipolar interactions of the scattering electron with different target states. The energy-dependent *R* matrix at the boundary is built from the energy-independent solutions from the inner region. Inside the inner region, this $(N+1)$ electronic wavefunction ψ_k^{N+1} is expressed as a close-coupling (CC) expansion,

$$\psi_k^{N+1} = A \sum_i \psi_i^N(x_1, \ldots, x_N) \sum_j \xi_j(x_{N+1}) a_{ijk} + \sum_m \chi_m(x_1, \ldots, x_{N+1}) b_{mk}, \quad (1)$$

where, in the first summation, ψ_i^N represents the wave function of the ith target state, u_{ij} are the continuum orbitals used to represent the scattering electron, and A is the antisymmetrization operator. The diagonalization of the inner-region Hamiltonian gives the variational coefficients a_{ijk} and b_{mk} in Eq. (1) and depends on the type of expansion for ψ_k^{N+1}. The second term χ_i^{N+1} gives the L^2 configurations, which have zero amplitude at the *R*-matrix interface. These L^2 configurations are generated by placing all the electrons in target molecular orbitals, and they allow relaxation of the orthogonalization enforced between the continuum orbitals and the target orbitals. Indeed, permitting the scattering electron to permeate unoccupied target molecular orbitals involved in the calculation is mandatory for completeness and to model high-l effects in the region of the target nuclei. In complex target models which consider the polarization of the molecule, like the static exchange plus polarization (SEP) model, the L^2 configurations also contribute in modeling the effects of target polarization in response to the scattering electron. The SEP model introduces electronically excited states into the calculations, and in principle allows the study of electron-impact electronic excitations. The present computations are all based on the SEP model.

The occupied and virtual molecular orbitals are constructed using the Hartree-Fock self-consistent-field method with Gaussian-type orbitals. The continuum is represented by the orbitals given by Faure *et al.* [36]. Only the orbitals up to $l = 4\,(g)$ are included in the present calculations. The presence of a permanent dipole moment for F_2CO requires that, to get a correct description of long-range interaction, inclusion of higher partial waves ($l > 4$) is necessary, and this may be implemented by applying a Born correction [25] at all energies, although this may overestimate the cross section at the lowest energies.

The *R* matrix on the boundary is expanded by the method defined by Gailitis [37] o obtain the asymptotic solutions in the outer region. The solution for the outer-region wave function is obtained in the form of **K** matrices. These **K** matrices provide all the physical observables which are used to compute cross sections. The eigenphase sum is also calculated from the eigenvalues of **K** matrices and can be represented as

$$\delta = \sum_i \arctan(K_{ij}) \quad (2)$$

RESON [38] is a resonance detection program which is used to determine the position and width of any resonance peaks. These resonance parameters are extracted from the eigenphase sum which matches a Breit-Wigner profile [39]. The cross sections are directly computed from **T** matrices which are derived from the **K** matrices. The standard relation which gives the total cross section using **T** matrices is written as

$$T = \frac{2iK}{1 - iK} \quad (3)$$

The POLYDCS program of Sanna and Gianturco [40] calculates the differential cross section (DCS) and the momentum transfer cross section (MTCS) at low energies. This suite includes a number of inputs including the **K** matrices, polarizabilities, dipole and quadrupole moments, incident electron energies, and the desired rotational transition. In this program, the body-fixed (BF) **K** matrices describing the electron-molecule collision at a given energy are read in from an external file and transformed into the space fixed (SF) frame of reference. The SF **K** matrices are then used to calculate state-to-state rotationally elastic and inelastic cross sections by summing the inelastic coefficients (A_L (L = orbital angular momentum)) [40] as a Legendre polynomial expansion. Linear, spherical, symmetric, and asymmetric rotors are evaluated with the inclusion of the Born correction [25] for polar molecular targets.

C. High-energy-formalism

High-energy total elastic and inelastic cross sections were modeled using the SCOP formalism [22–25]. The total ionization cross section is derived from the total inelastic cross section by a semiempirical CSP-ic method [29–31]. In the SCOP method, the spherical part of the complex optical potential is treated exactly in the partial-wave analysis. The

complex potential calculation for electron scattering provides total elastic cross sections $Q_{\rm el}$ and their counterpart total inelastic cross sections $Q_{\rm inel}$ such that the total scattering cross section (TCS) is given by

$$Q_T(E_i) = Q_{\rm el}(E_i) + Q_{\rm inel}(E_i). \quad (4)$$

Our calculation for the TCS is based on complex scattering potentials, generated from spherically averaged charge densities of the target. The molecular charge density is employed to construct a complex optical potential $V_{\rm opt}$, given by

$$V_{\rm opt}(r, E_i) = V_R(r, E_i) + i\, V_{\rm abs}(r, E_i). \quad (5)$$

The real part V_R is comprised of static potential ($V_{\rm st}$), exchange ($V_{\rm ex}$), and polarization (V_p) terms, summed as follows:

$$V_R(r, E_i) = V_{\rm st}(r, E_i) + V_{\rm ex}(r, E_i) + Vp(r, E_i). \quad (6)$$

The analytical form of the static potential is derived using the Hartree-Fock wave functions of Cox and Bonham [41]. For the exchange potential, we have used the parameter-free free-electron-gas exchange model of Hara [42]. For the polarization potential V_p, the parameter-free model of the correlation polarization potential is used, which contains multipole nonadiabatic corrections in the intermediate region and smoothly approaches the correct asymptotic form for large r, given by Zhang *et al.* [43].

The imaginary part (absorption potential $V_{\rm abs}$) accounts for the total loss of scattered flux into all the allowed channels of electronic excitation and ionization. The quasifree model potential given by Staszewska *et al.* [44] is employed for $V_{\rm abs}$; it has a Pauli blocking and dynamic form. After generation of the full complex potential given in Eq. (5) for a given electron-molecule system, the Schrödinger equation is solved numerically using partial-wave analysis. At low incident electron energies only a few partial waves are significant, but as the incident energy increases, more and more partial waves will be required for convergence. Using these partial waves, complex phase shifts are obtained which are employed to find the relevant cross sections using Eqs. (8) and (9). In the present calculation the nonspherical terms such as vibrational and rotational potentials are neglected in the full expansion of the optical potential since contributions from these terms are low at the intermediate and high energies. The phase shifts (δ_l) obtained are then employed to find the inelasticity or absorption factor η_l:

$$\eta_l = \exp(-2{\rm Im}\delta_l) \quad (7)$$

The total elastic ($Q_{\rm el}$), and the total inelastic ($Q_{\rm inel}$) cross sections may then be computed from η_l:

$$Q_{\rm el}(E_i) = \frac{\pi}{k^2} \sum_{l=0}^{\infty} (2l+1)\, |\eta_l \exp({\rm Re}\delta_l) - 1|^2 \quad (8)$$

and

$$Q_{\rm inel}(E_i) = \frac{\pi}{k^2} \sum_{l=0}^{\infty} (2l+1)\big(1 - \eta_l^2\big). \quad (9)$$

The total scattering cross section Q_T is obtained by adding these two cross sections together. Rather than the inelastic cross section which is calculated above, it is the ionization cross section which has much more significance in the applied field; absolute ionization cross sections are more easily measured and, as such, provide a more accurate reference for comparison with theory. In order to deduce the ionization contribution from its inelastic counterpart, a semiempirical method is employed (CSP-ic [29–31]). This method invokes an approximate and dynamic ratio of the ionization cross section to the inelastic cross section. Since the inelastic cross section has already been calculated using the SCOP method, the ionization cross section can be extracted from the inelastic part through this ratio. The details of constructing the ratio and the derivation of the ionization cross section from the ratio are explained in our previous works [29–31].

TABLE II. Total cross section (TCS) for the electron scattering from F_2CO (energies are in eV and TCSs are in Å^2).

Energy	TCS	Energy	TCS	Energy	TCS	Energy	TCS	Energy	TCS
0.5	90.22	4	27.13	12	19.44	24	20.11	300	7.64
0.6	77.97	4.5	24.81	13	19.23	26	19.75	400	6.83
0.7	69.09	5	23.76	14	20.37	28	18.77	500	6.20
0.8	62.37	5.5	22.92	15	21.24	30	17.64	600	5.69
0.9	57.10	6	22.21	16	20.88	40	14.12	700	5.25
1	52.86	6.5	21.60	17	20.34	50	13.31	800	4.88
1.2	46.50	7	21.10	18	19.82	60	13.22	900	4.56
1.5	40.16	7.5	20.71	19	19.44	70	13.05	1000	4.28
2	33.92	8	20.42	20	19.29	80	12.73	2000	2.64
2.5	30.27	9	20.16	22	19.51	90	12.34	3000	1.91
3	28.03	10	20.06	24	19.75	100	11.99	4000	1.50
3.5	29.79	11	19.86	26	18.45	200	8.90	5000	1.25

III. RESULTS AND DISCUSSION

The present work provides a comprehensive set of electron-impact cross sections for F_2CO over a wide energy range (0.5 to 5000 eV). The numerical values of total cross sections obtained for F_2CO are listed in Table II for ready reference and are also plotted graphically in Fig. 3.

The TCS for different symmetry components in electron scattering by F_2CO is plotted in Fig. 2. It can be seen that the maximum contribution from the TCS comes from the $^2B_1$ symmetry component of the C_{2v} point group. The shape resonance appearing for the $^2B_1$ symmetry is clearly indicated in the TCS curve (Fig. 3). Moreover, we see that the resonance appearing due to the static exchange (SE) approximation lies at a higher energy than the resonance due to static-exchange plus polarization (the SEP model). The high magnitude of the cross section at very low energies is contributed mainly by the $^2A_1$ symmetry component of the C_{2v} point group. It may be noted here that the long-range potential can influence the magnitude of the cross section at low energies due to the $l = 0$ partial wave. The other two symmetries, $^2B_2$ and $^2A_2$ have only small-magnitude TCSs, so their cross section scales are magnified to give a better view of their cross section variation with energy.

Figure 3 shows the TCS curve of F_2CO over a wide energy range from 0.5 to 5000 eV. Amalgamation of the R-matrix and SCOP formalisms allows the total cross sections to be

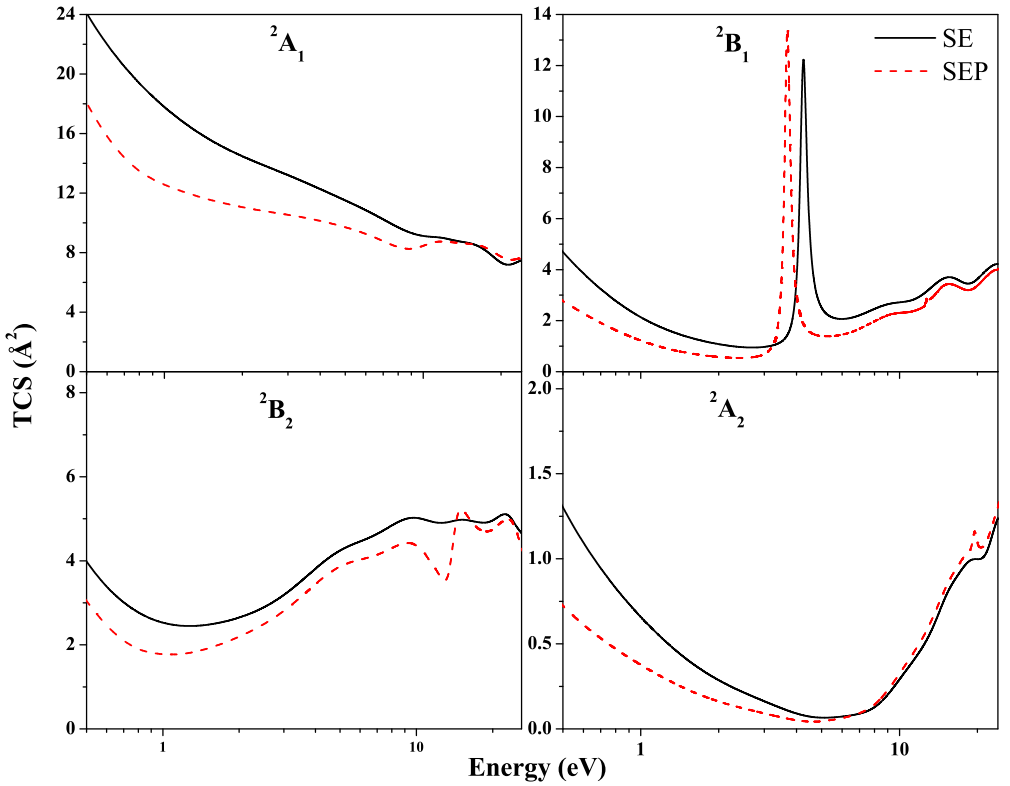

FIG. 2. (Color online) Symmetry components of the TCS for e-F_2CO scattering.

determined over a wide energy range. The TCS curve shows a sharp feature at 3.67 eV for the SEP and 4.23 eV for the SE approximation, which is a shape resonance appearing in the electron F_2CO interaction. This shape resonance is of π^* character and is located on the double bond (C = O) of the F_2CO molecule. As seen from the curve, the identified resonance is located at a higher energy for the SE model as compared to that of the SEP model. The occurrence of resonance at such low energies signifies the temporary binding of electrons within the unoccupied molecular orbitals or excitation of the occupied molecular orbitals. This is termed dissociative electron attachment. Morgan [45] has described DEA as a pivotal process occurring in various low-energy plasma as it is the primary step which leads to the breakup of feed stock gases into radicals and ions in the technological plasmas used in the plasma processing industry. Thus, a DEA process is a crucial step in understanding and modeling plasma processing procedures [46]. DEA may consequently lead to the fragmentation of the molecule into either neutral or anionic species. Hoshino *et al.* [19] located three DEA products (F^-, F_2^-, COF^-) in the energy range from 0.75 to 2.62 eV with the help of Gaussian fitting profiles and an energy resolution of 0.5 eV. However, we have a found a shape resonance at an energy nearly 1 eV greater than that observed by Hoshino *et al.* [19]. The electron beam resolution used by Hoshino *et al.* [19] in their measurements is lower, which may mask some resonances. Furthermore it is common for SE and SEP models to place resonances at higher energies than experiment.

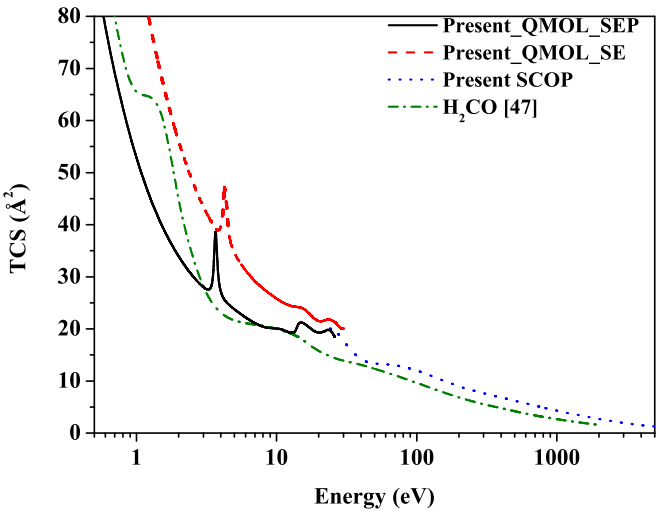

FIG. 3. (Color online) TCS for e-F_2CO scattering.

Since there appears to be a lack of experimental measurements of the F_2CO total scattering cross section, we compare the present data with the TCS of H_2CO, whose H atoms are replaced by F atoms in F_2CO. A detailed TCS calculation for H_2CO has been reported by Vinodkumar *et al.* [47]. It is observed that the resonance peak is shifted in the TCS of F_2CO as compared to the TCS of H_2CO. The TCS curve also contains broader peaks at around 20 eV, after which it decreases monotonically with increasing energy. Here, the TCS is the sum of elastic and inelastic channels. The convergence of the elastic cross sections in terms of the number of excited states included in the open-channel space is achieved quickly. The probability flux into the elastic channel decreases as more open channels are added in the calculation, hence leading

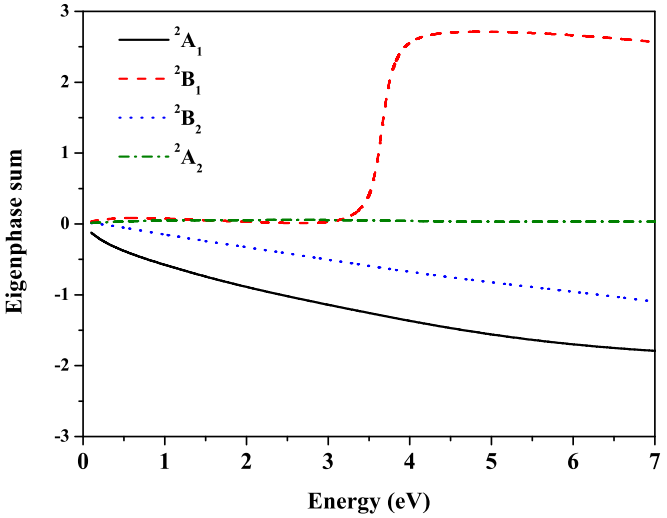

FIG. 4. (Color online) Doublet eigenphase sum for e-F_2CO scattering.

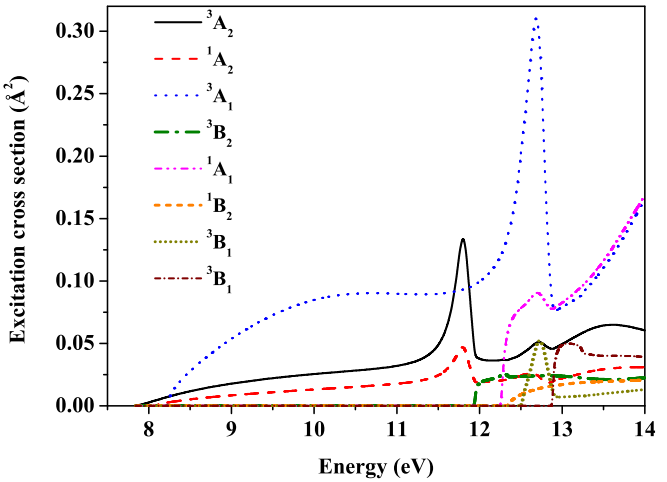

FIG. 5. (Color online) Electronic excitation cross section for e-F_2CO scattering to different singlet and triplet states.

to a marked decrease in the magnitude of the corresponding cross sections. This effect becomes even more important for higher impact energies. As the elastic cross section decreases due to the presence of more open channels, the TCS drops accordingly, as seen in Fig. 3.

Eigenphase diagrams provide the positions of resonances. Resonance positions occur at distinct energies and are crucial to understanding low-energy electron scattering dynamics. A resonance may decay, leading to the dissociation of the molecule into either neutral or anionic fragments or leave the target molecule in the vibrationally excited state after the ejection of the impinging electron. The RESON program [38] employs a recursive procedure for detecting and performing Breit-Wigner fits to the eigenphase diagram. The resonance parameters, i.e., the position and width of the resonance, are obtained from these fits. Figure 4 show the eigenphase sum for various states of the F_2CO molecule. The eigenphase sum plot of F_2CO molecule clearly attributes the low-energy shape resonance observed at 3.67 eV to $^2B_1$ symmetry of the molecule.

Figure 5 presents electron-impact excitation cross sections to various singlet and triplet excited states. The threshold of excitation for the first singlet and triplet excitations are evaluated at 8.092 and 7.282 eV, respectively. The triplet excitations contribute more than their corresponding singlet excitations due to the large spin multiplicity and lower thresholds of triplet states. Hence, the cross sections for triplet states are larger than the corresponding singlet states. There has been much work on the vertical excitation spectrum of F_2CO. Table III lists selected vertical excitation states compared with the data of Vasudevan and Grein [11], Grein [13], and Kato *et al.* [16]. Kato *et al.* [16] have only reported the excitation energies of singlet states. The present values are in good agreement with the values reported by Grein [13] and Kato *et al.* [16]. However, the values reported by Vasudevan and Grein [11] are lower than the present and other reported values. The assignment of the transitions in various orbitals is given in detail for singlet states by Kato *et al.* [16] and for singlet and triplet states by Grein [13]. For the present reported values of excitation energies, the configurations corresponding to different states are mentioned in Table III. The $\pi\pi^*$ transition has the highest oscillator strength [13], which corresponds to transition to $^3A_1$ and contributes most to the excitation cross section curve (Fig. 5).

Figure 6 shows the differential elastic cross sections for incident energies 1, 3, 6, 9, 12, and 15 eV over scattering angles between 0° and 180°. The DCS curves at different energies are plotted in the same figure as there are no comparisons, theoretical or experimental, available in the literature to the best of our knowledge. F_2CO has a permanent dipole moment which contributes to the large values of DCS at forward scattering angles. This large amplification in the forward direction is attributed to the dipolar nature of the strong long-range interaction potential. The differential cross section decreases in magnitude at forward angles. However, at backward angles, some oscillations may appear in the cross section curve. These oscillations occur in the DCS due to the coupling of higher partial waves used in the calculation. The oscillations present in the DCS curve reflect the partial-wave

TABLE III. Present vertical excitation states of a few selected target states with available comparisons.

State	Present	Vasudevan and Grein [11]	Kato *et al.* Grein [13]	Kato *et al.* [16]	Configuration
$^1A_1$	0	0	0	0	Ground state
$^3A_2$	7.28	6.59	7.01		$n_o\pi*$
$^1A_2$	8.09	6.87	7.35	7.47	$n_o\pi*$
$^3A_1$	8.23	7.04	7.36		$\pi\pi*$
$^3B_2$	11.94	10.37	11.94		n_o4s
$^1A_1$	12.27	10.89	12.19	12.37	$\pi 3p_x$
$^1B_2$	12.34	11.27	11.88	12.22	$n_0 3d_{x^2-y^2}$
$^3B_1$	12.51		12.42		$\pi 3p_z$
$^3B_1$	12.89		12.75		$\pi 3d_{z^2}$
$^1B_1$	13.23		12.41	12.60	$\pi 3p_z$
$^1B_1$	13.35		13.26	13.48	$\pi 3d_{x^2-y^2}$

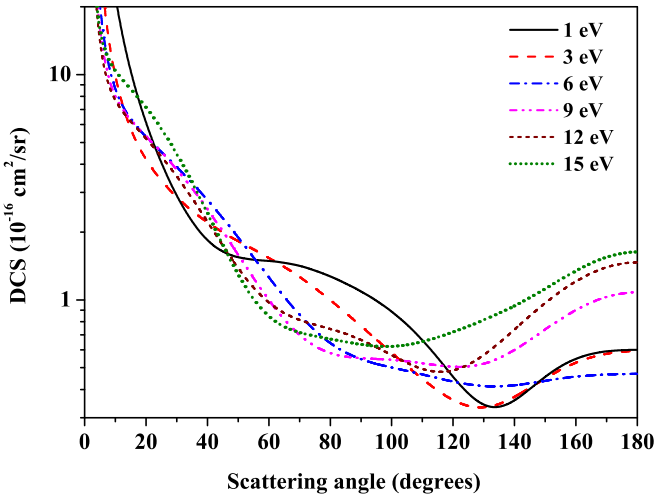

FIG. 6. (Color online) Differential elastic cross section for e-F_2CO scattering at energies from 1 to 15 eV.

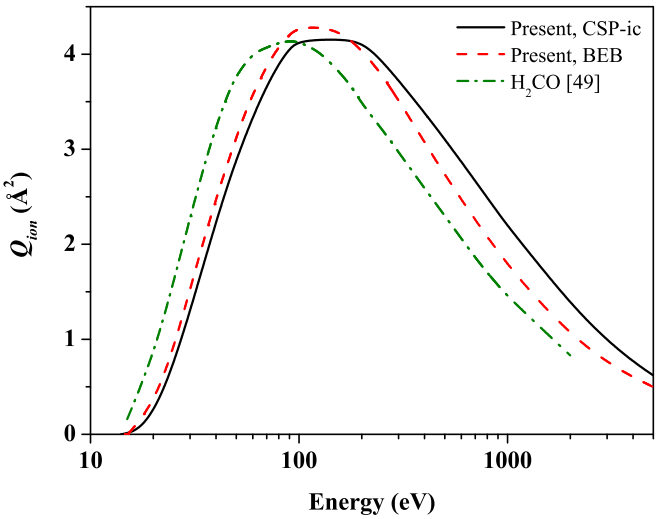

FIG. 8. (Color online) Total ionization cross section for e-F_2CO scattering.

contribution. The DCS curves present two minima for some energies, a feature of d-wave scattering.

Momentum transfer cross sections for electron-F_2CO scattering between 0.5 and 11 eV are shown in Fig. 7. MTCSs are calculated from DCSs as they are the elastic cross sections weighted by a factor of $1-\cos\theta$. The MTCSs indicate the importance of the backward angle scattering and are an important input to solve the Boltzmann equation. The MTCS is useful in defining the drift of electrons under an applied electric field through a molecular gas. Several transport observables such as the diffusion coefficient D and mobility μ can be obtained from MTCS data. The momentum transfer cross sections are also used to calculate the effective collision frequency over a wide electron temperature range.

Figure 8 compares the total ionization cross section ($Q_{\rm ion}$) for e-F_2CO scattering obtained using the complex scattering potential–ionization contribution method and using the binary encounter Bethe (BEB) method developed by Kim and Rudd [48]. The calculations for $Q_{\rm ion}$ is performed from the vertical ionization potential of the target (13.62 eV) to 5 keV. The

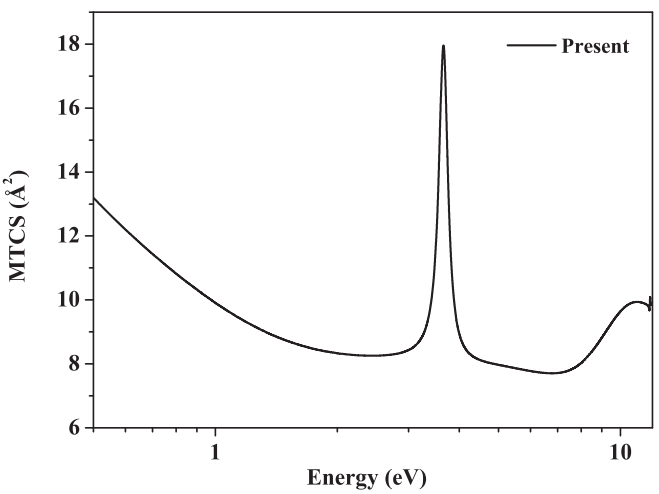

FIG. 7. e-F_2CO momentum transfer cross section.

$Q_{\rm ion}$ is derived from the total inelastic cross section through a dynamic ratio as explained earlier. The present ionization curve agrees quite well with the computed BEB data [48] below the peak. However, the BEB peak rises and falls faster than the peak calculated using the CSP-ic [25–27] method The present data are also compared with those for H_2CO [49] as in the case of the TCS. The peak position in this case is also found to be shifted as F_2CO has a higher ionization potential than H_2CO.

IV. CONCLUSION

To date there are few electron-impact cross section studies of carbonyl fluoride; however, since it is considered an important molecule due to its low GWP and its application as a chamber cleaning agent, electron interactions with this molecule are becoming important in understanding its local chemistry in the different environments it is used in. This paper reports the total electron scattering cross section, differential cross section, electronic excitation cross section, momentum transfer cross section, and ionization cross section for the F_2CO molecule using two formalisms. At low impact energies, the *ab initio* R-matrix method was utilized through the QUANTEMOL-N software while at high energies the SCOP and CSP-ic formalisms were employed for TCS and ionization cross section calculations, respectively. The data computed using the two formalisms are consistent. Thus, the amalgamation of two formalisms can produce a robust data set for electron-molecule collision. Since there is apparently no cross section dataset available in the literature for this molecule, the present total and total ionization cross sections are compared with the data for H_2CO, which is structurally similar to F_2CO. A shift in peak and a higher magnitude in cross section in the ionization cross section are observed in the case of F_2CO due to the presence of fluorine.

The computed target properties such as the ground-state energy, first electronic excitation energy, dipole moment, and rotational constant were found to agree well with the predicted theoretical and experimental results, as evident from Table I. The present vertical electronic spectrum is in good accord

with available comparisons. The present prediction of a shape resonance is centered at 3.67 eV for the SEP model and 4.23 for the SE model and appears as a sharp feature in the TCS curve.

ACKNOWLEDGMENT

B.K.A. is pleased to acknowledge the support of this research by the Science & Engineering Research Board (SERB), New Delhi, through Grant No. SB/S2/LOP-011/2013.

[1] J. Franklin, Chemosphere **27**, 1565 (1993).
[2] Y. Mitsui, Y. Ohira, T. Yonemura, T. Takaichi, A. Sekiya, and T. J. Beppu, J. Electrochem. Soc. **151**, G297 (2004).
[3] M. Riva, A. E. Lopez, D. Linaschke, I. Dani, and S. Kaskel, Patent No. WO 2011032983 A2, US, March 24 (2011).
[4] T. S. Dibble, M. M. Maricq, J. J. Szente, and J. S. Fransciso, J. Phys. Chem. **99**, 17394 (1995).
[5] D. E. Milligan, M. E. Jacox, A. M. Bass, J. J. Comeford, and D. E. Mann, J. Chem. Phys. **42**, 3187 (1965).
[6] G. L. Workman and A. B. F. Duncan, J. Chem. Phys. **52**, 3204 (1970).
[7] V. W. Laurie and D. T. Pence, J. Mol. Spectrosc. **10**, 155 (1963).
[8] V. W. Laurie, D. T. Pence, and R. H. Jackson, J. Chem. Phys. **37**, 2995 (1962).
[9] J. Overend and J. R. Scherer, J. Chem. Phys. **32**, 1296 (1960).
[10] R. F. Miller and R. F. Curl Jr., J. Chem. Phys. **34**, 1847 (1961).
[11] M. B. Robin, *Higher Excited States of Polyatomic Molecules* (Academic Press, New York, 1975), Vol. 2.
[12] K. Vasudevan and F. Grein, Int. J. Quantum Chem. **14**, 717 (1978).
[13] P. Sherwood, E. A. Seddon, M. F. Guest, M. J. Parkington, T. A. Ryan, and K. E. Seddon, J. Chem. Soc. Dalton Trans. **103**, 2359 (1995).
[14] F. Grein, J. Phys. Chem. **102**, 10869 (1998).
[15] E. Olalla, C. Lavín, A. M. Velasco, and I. Martín, Chem. Phys. Lett. **366**, 477 (2002).
[16] H. Choi and K. K. Baeck, Mol. Phys. **103**, 2247 (2005).
[17] H. Kato, C. Makochekanwa, M. Hoshino, M. Kimura, H. Cho, T. Kume, A. Yamamoto, and H. Tanaka, Chem. Phys. Lett. **425**, 1 (2006).
[18] H. Kato, Y. Nunes, D. Duflot, P. Limao-Vieira, and H. Tanaka, J. Phys. Chem. A **115**, 2708 (2011).
[19] M. Hoshino, P. Limão-Vieiraa, M. Probst, Y. Nunes, and H. Tanaka, Int. J. Mass Spectrom. **303**, 125 (2011).
[20] J. Tennyson, Phys. Rep. **491**, 29 (2010).
[21] J. Tennyson, D. B. Brown, J. J. Munro, I. Rozum, H. N. Varambhia, and N. Vinci, J. Phys.: Conf. Ser. **86**, 012001 (2007).
[22] A. Jain and K. L. Baluja, Phys. Rev. A **45**, 202 (1992).
[23] M. Vinodkumar, A. Barot, and B. K. Antony, J. Chem. Phys. **136**, 184308 (2012).
[24] D. Gupta, R. Naghma, B. Goswami, and B. K. Antony, RSC Adv. **4**, 9197 (2014).
[25] J. Kaur, B. Goswami, D. Gupta, and B. K. Antony, Phys. Rev. A **90**, 012711 (2014).
[26] K. Takatsuka and V. McKoy, Phys. Rev. A **24**, 2473 (1981); **30**, 1734 (1984).
[27] T. N. Rescigno and B. I. Schneider, Phys. Rev. A **45**, 2894 (1992); T. N. Rescigno, B. H. Lengsfield, C. W. McCurdy, and S. D. Parker, *ibid.* **45**, 7800 (1992).
[28] B. I. Schneider and L. A. Collins, J. Phys. B: At. Mol. Phys. **14**, L101 (1981).
[29] J. Kaur, R. Naghma, and B. K. Antony, RSC Adv. **5**, 20090 (2015).
[30] D. Gupta and B. K. Antony, J. Chem. Phys. **141**, 054303 (2014).
[31] B. Goswami, R. Naghma, and B. Antony, Int. J. Mass Spectrom. **372**, 8 (2014).
[32] http://www.cccbdb.nist.gov/
[33] G. Herzberg, *Electronic Spectra and Electronic Structure of Polyatomic Molecules* (Van Nostrand, New York, 1966).
[34] R. D. Nelson Jr., D. R. Lide Jr., and A. A. Maryott, "Selected values of electric dipole moments for molecules in the gas phase," National Standard Reference Data Series—National Bureau of Standards 10 (NSRDS-NBS10) September 1 (1967), http://www.nist.gov/data/nsrds/NSRDS-NBS-10.pdf.
[35] S. H. D. M. Faria, J. V. da Silva, Jr., R. L. A. Haiduke, L. N. Vidal, P. A. M. Vazquez, and R. E. Bruns, J. Phys. Chem. A **111**, 7870 (2007).
[36] A. Faure, D. Gorfinkiel, L. A. Morgan, and J. Tennyson, Comput. Phys. Commun. **144**, 224 (2002).
[37] M. Gailitis, J. Phys. B **9**, 843 (1976).
[38] J. Tennyson and C. J. Noble, Comput. Phys. Commun. **33**, 421 (1984).
[39] G Breit and E. Wigner, Phys. Rev. **49**, 519 (1936).
[40] N Sanna and F. A. Gianturco, Comput. Phys. Commun. **114**, 142 (1998).
[41] H. L. Cox and R. A. Bonham, J. Chem. Phys. **47**, 2599 (1967).
[42] S. Hara, J. Phys. Soc. Jpn. **22**, 710 (1967).
[43] X. Zhang, J. Sun, and Y. Liu, J. Phys. B **25**, 1893 (1992).
[44] G. Staszewska, D. W. Schwenke, D. Thirumalai, and D. G. Truhlar, Phys. Rev. A **28**, 2740 (1983).
[45] W. Morgan, Adv. At. Mol. Opt. Phys. **43**, 79 (2000).
[46] M. Kimura, Adv. At. Mol. Opt. Phys. **44**, 33 (2001).
[47] M. Vinodkumar, H. Bhutadia, B. Antony, and N. Mason, Phys. Rev. A **84**, 052701 (2011).
[48] Y. K. Kim and M. E. Rudd, Phys. Rev. A **50**, 3954 (1994).
[49] M. Vinodkumar, K. N. Joshipura, C. Limbachiya, and N. Mason, Phys. Rev. A **74**, 022721 (2006).